ACTA METALLURGICA SLOVACA
2023, VOL. 29, NO. 2, 82-87

RESEARCH PAPER

CHANGE IN MICROSTRUCTURE AND HARDNESS OF ADDITIVELY MANUFACTURED AISI H13 STEEL BY HEAT TREATMENT AND NITRIDING PROCESSES

Son Anh Nguyen[1], Khanh Gia Pham[2], Christian Seidel[2], Anh Hoang Pham[3], Cuong Nhu Phung[1], Trung Van Trinh[1,]*

[1] School of Materials Science and Engineering, Hanoi University of Science and Technology, No.1, Dai Co Viet, Hanoi, Vietnam
[2] Department of Applied Sciences and Mechatronics, Munich University of Applied Sciences, Lothstr. 34, Munich, Germany
[3] Faculty of Materials for Energy, Shimane University, Matsue, Shimane, Japan

*Corresponding author: trung.trinhvan@hust.edu.vn, tel.: +84 24 38680409, Hanoi University of Science and Technology, 100000, Ha Noi, Vietnam

Received: 15.02.2023
Accepted: 17.04.2023

ABSTRACT

AISI H13 steel samples were additively manufactured using a laser powder bed fusion (LPBF) system. The effect of annealing temperature, quenching & tempering, and nitriding were determined. The microstructure and properties of the samples were investigated using optical microscopy, scanning electron microscopy, electron backscattered diffraction, electron probe micro-analysis, X-ray diffraction, roughness measurement, and a hardness tester. The results show that the as-built AISI H13 steel sample had a roughness on the surface and pores inside. The microstructure consisted of martensite and retained austenite. The average hardness was 460 HV, and the porosity was 0.086 %. The annealing process helped homogenize the microstructure, increase the density, and reduce the porosity and hardness of the LPBF-manufactured sample. The quenching process helped increase the hardness of the steel to the maximum of 787 HV, then the tempering process reduced the hardness to 572 HV. Heat treatment and nitriding processes tended to increase the martensite block size, reduce the retained austenitic content, and precipitate the V-Mo-rich carbide in the LPBF-manufactured AISI H13 steel. After nitriding was conducted, the nitriding case depth was 87 μm, and the surface hardness increased up to higher than 1020 HV due to the formation of CrN and $Fe_{3-4}N$.

Keywords: Laser powder bed fusion (LPBF); AISI H13 steel; heat treatment; gas nitriding

INTRODUCTION

Additive manufacturing technology is increasingly being applied to make parts based on metal materials, such as AISI H13 steel and aluminium alloy, for industrial applications [1-5]. H13 is a steel that is commonly used for die-casting moulds. Some AM techniques have been studied and implemented for this steel, including laser powder bed fusion (LPBF) technology. The structure and properties of the printed part depend heavily on the input parameters, such as the material; the printing technology; and the post-printing processes, such as heat and surface treatment [6-8]. Applying preheating during the LPBF process results in a more homogeneous microstructure of the material with better mechanical properties than those without preheating [9]. Hot isostatic pressing (HIP) post-treatment improved the density of the LPBF-fabricated part [10]. Heat treatment could contribute to reducing residual stress and porosity and make the microstructure homogenized for additively manufactured steel [11-13]. Low-temperature annealing (350–650) °C for 2 h for additively manufactured H13 steel was carried out by C. J. Chen [14]. The result showed induction in the further phase transformation of martensite into tempered martensite with the precipitation of carbides, leading to a slight increase and finally a sharp decrease in hardness with increasing temperature. Due to the nature of additively manufactured objects and the fast cooling rate, they have heterogeneous and anisotropic structures, as well as the existence of many defects (such as dislocation, crack, pore, and balling effect), low density, and uneven precipitation of carbide phases between regions of the melt pool in the additively manufactured object, high-temperature annealing studies should be conducted to homogenize the microstructure, eliminate residual stress, and reduce defect density [15]. Quenching and tempering processes could help tailor a steel's microstructure and mechanical properties to specific applications [15]. HIP before quenching and tempering (Q&T) for hot-work tool steel manufactured by laser powder bed fusion significantly increased the impact toughness and ductility and slightly increased the yield and ultimate tensile strength values compared with the Q&T condition [16]. Besides, nitriding technology could help improve the surface hardness of steel [16-18]. However, the change of phases and hardness of additively manufactured H13 steel during heat and surface treatment processes including high-temperature annealing, quenching, tempering, and nitriding has not been demonstrated in the literature. The present study aimed to investigate the effect of high-temperature annealing (860–1020) °C, Q&T, and gas nitriding processes on the microstructure and properties of the as-received LPBF-manufactured H13 steel. Further studies on the martensite's morphology change, the retained austenite's distribution, and the carbide formation in the LPBF-manufactured H13 steel after tempering and nitriding

were also conducted by electron backscattered diffraction (EBSD) and electron probe microanalyzer (EPMA).

MATERIAL AND METHODS

AISI H13 hot work tool steel samples ($10 \times 10 \times 25$ mm^3) were additively manufactured using an LPBF system (AL-METAL 250) from the company Alpha Laser (Puchheim, Germany). The manufacturing was performed in an Ar-protected environment using MetcoAdd H13-A powder. The martensitic, iron-chromium MetcoAdd H13-A steel powder produced by the gas atomization technique showed a well-spheroidal shape that enables optimized spreadability and dense packing. The chemical properties and particle-size distribution of the powder are presented in **Tables 1** and **2**.

Table 1 Chemical composition of MetcoAdd H13-A powder [19]

Powder	Weight Percent (%)					
	Fe	*Cr*	*Mo*	*Si*	*V*	*C*
MetcoAdd H13-A	Balance	5.2	1.3	1.0	1.0	0.4

Table 2 Particle size distribution of MetcoAdd H13-A powder [19]

Powder	Nominal Range [µm]	D90 [µm]	D50 [µm]	D10 [µm]
MetcoAdd H13-A	-45 +15	50	34	21

The LPBF process was carried out with the following parameters:

- powder layer thickness: 50 µm,
- hatching distance: 50 µm,
- laser power: 136 W,
- laser wavelength: 1070 nm,
- laser focus diameter: 50 µm, and
- scan speed: 1133 mm/s.

The effect of annealing temperatures of 860 °C, 920 °C, 980 °C, and 1020 °C for 4 h was determined. The samples were also quenched in a vacuum furnace with N_2 gas with a pressure of 5.3 bar from an austenitization temperature of 1030 °C at a soaking time of 1.5 h and then tempered at 585 °C for 5 h. The as-built and heat-treated samples were then nitrided at 520 °C for 3 h by using a mixture of NH_3 and N_2 gas. The abbreviation of the samples at different states is listed in **Table 3**.

Table 3 Sample state and corresponding abbreviation

Sample state	Abbreviation
As-printed	AM
Annealing at 860 °C	A860
Annealing at 920 °C	A920
Annealing at 980 °C	A980
Annealing at 1020 °C	A1020
Quenching	Q
Quenching and tempering	Q&T
As-printed + nitriding	AM + N
Quenching and tempering + nitriding	AM + Q&T + N

Nital etching solution was used to etch specimens for microstructural observations. Optical microscopy (AXIOVERT 25CA), digital optical microscopy (VHX-7000), scanning electron microscopy (SEM, JSM-IT200) with energy-dispersive spectrometry (EDS), precision roughness measurement (SURFCOM NEX 001), X-ray diffraction (Aeris Research) with Cu Kα radiation, micro-hardness testing (Struers Duramin 2) with 50 g load for 15 s, and porosity and density measurements (Archimedes method) were applied to investigate the microstructure and properties of the samples. The morphology of martensite and the distribution of retained austenite in the samples were investigated by electron backscattered diffraction (EBSD). The samples were cross-sectionally cut along the building plane, mechanically polished down to 1 µm diamond spray, and finished with 50 nm colloidal silica suspension. The EBSD measurement was performed on JEOL JIB-4700F FESEM equipped with a Symmetry S2 EBSD detector from Oxford Instruments. The position of the EBSD measurement was near the sample centre. Its conditions were 20 kV voltage, 10 nA probe current, and 0.1 µm step square grid. Elemental mapping of the samples was also performed using wavelength dispersive spectroscopy (WDS) in a field-emission electron probe microanalyzer (JEOL JXA-8530F Plus EPMA) to investigate the carbide formation in the samples. The measurement conditions were 15 kV, 50 nA, and 0.4 µm probe diameter.

RESULTS AND DISCUSSION

Fig. 1 shows the surface analysis of the as-built sample. Many red dots could be seen on the digital optical microscopic image (**Fig. 1a**), indicating corrosion on the surface of the as-built steel after SLM. The corrosion resistance of LPBF-fabricated samples is influenced by the microstructure and the surface status such as grain size, second phase precipitation, voids, residual stress, and surface roughness et al., which are strongly affected by the parameters such as the input energy density and the cooling rate of the printing process [20, 21]. The surface was rough, with a Ra of about 7.982 µm (**Fig. 1b**), because residual powder particles were embedded on the top surface (**Fig. 1c**). Surface roughness is the feature of LPBF-based production due to insufficient melting of the powder particles on the powder bed and balling effect [15]. Surface roughness upon LPBF is normally higher than that of machined surfaces, which is related to both sequential stacking of layers and partially melted powder particles adhering to the part surface. Additional milling, deep rolling, grinding and polishing processes can be applied to reduce the surface roughness of LPBF-fabricated objects [22, 23]. The heat treatment and the nitriding post-treatments resulted in a slight increase in surface roughness [16]. The chemical composition at the point of analysis of the unmelted powder particle by EDS (**Fig. 1d**) was similar to that of the steel powder. After the built surface was polished, a columnar structure with about 30 µm thickness oriented along the laser scan direction was observed in a cross-section perpendicular to the building direction (**Fig. 1e**). In a cross-section parallel to the building direction, the melt pools could be seen as “fish fins” with a fusion depth of more than 50 µm (**Fig. 1f**). The X-ray diffraction results (**Fig. 1g**) showed the existence of martensite and retained austenite in the as-built sample. Due to the layer-by-layer printing process, the material is subjected to melting, rapid cooling and thermal cycling. The solidification of the material starts with the formation of prior austenite colonies. During the rapid cooling, martensite is formed within these prior austenite colonies [16]. This is again due to the high cooling rate that can suppress carbide precipitation, allowing more alloy elements to dissolve in austenite, which reduces the martensite start transformation temperature, thus resulting in retained austenite in the printed sample. The SEM image in **Fig. 1h** showed the existence of pores in the as-printed sample. These pores decreased the strength and elongation of the LPBF-fabricated steel [24].

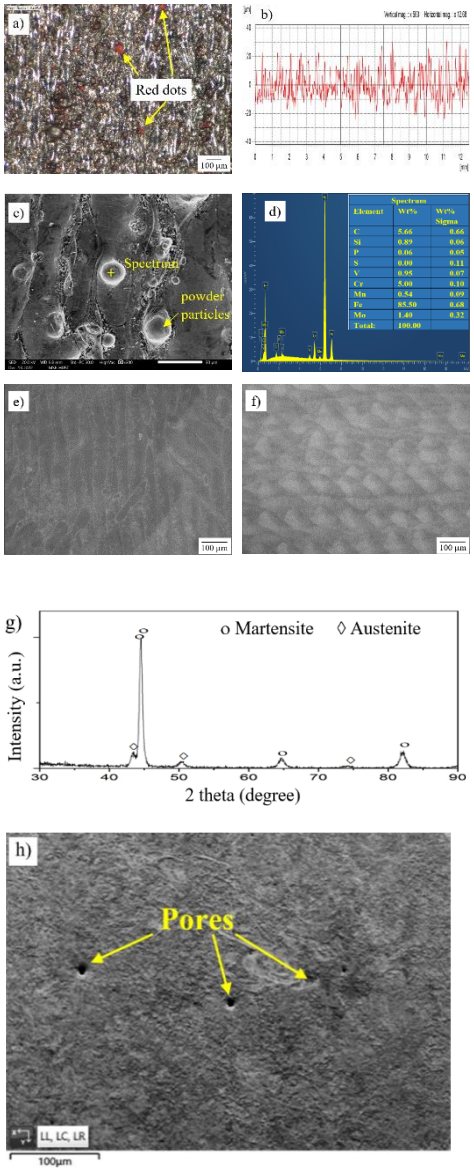

Fig. 1 Surface analysis of AM sample by a) digital optical microscopy, b) precision roughness measurement, c) scanning electron microscopy (SEM) and d) point EDS analysis of the unmelted powder particle on the as-received sample; optical microscopy on e) cross-section and f) along the building direction; g) X-ray diffraction; and h) SEM of the polished sample.

Fig. 2 shows the microstructure (on the section perpendicular to the building direction of the parts) of the as-built, annealed, quenched, and tempered samples. In the as-built state (**Fig. 2a**), the fusion lines had a size of about 50 µm, corresponding to the size of the laser beam when printing. Some pores were observed in the microstructure of the as-built steel (**Fig. 2b**), and they disappeared after annealing at high temperatures (**Figs. 2c–f**). The presence of pores can initiate cracks and result in an uneven distribution of stress across the material's cross-section, potentially affecting its mechanical properties. The effects depend on various factors, including the number of pores, their interconnection, size, morphology, and distribution [25-27]. For the as-received sample, the density was 7.907 g/cm^3, and the porosity was 0.086 %. B. Almangour et al. [10] believe that the driving force for porosity is associated with the gas flow caused by evaporation when a laser irradiates the metal powder, which in turn clears away powder near the laser's path during the build. This "denudation" phenomenon can reduce the amount of powder available when the laser makes its next building pass, causing tiny gaps and defects in the finished part. Besides, the balling effect hinders the uniform deposition of fresh powder on the previously sintered layer and often leads to porosity [15]. The annealing process helped increase the density and reduce the porosity. The porosity reduction led to an increase in the ductility of the LPBF-fabricated samples [16]. After annealing was performed at 1020 °C for 4 h, the density was 7.958 g/cm^3, and the porosity was 0.020%. After the high-temperature annealing treatment, the martensite formed in the AM sample was decomposed to ferrite and carbides [8]. Martensites were formed after quenching and were turned into tempered microstructure after tempering (**Figs. 2g** and **h**).

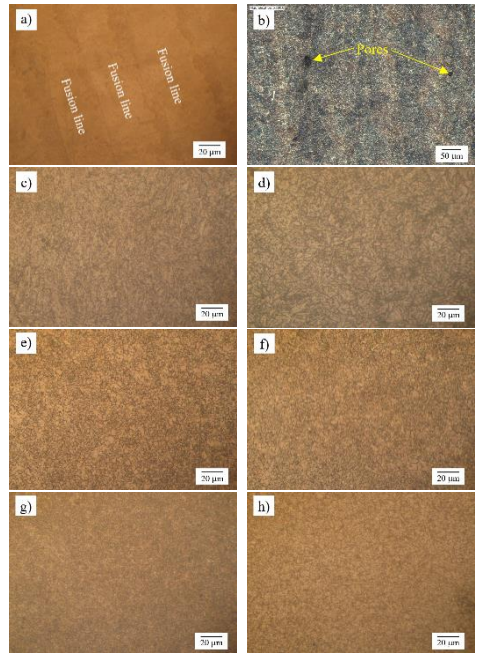

Fig. 2 a) Optical microscopic and b) digital optical microscopic images of AM sample and optical microscopic images of A860, d) A920, e) A980, f) A1020, g) Q and h) Q&T samples

Fig. 3 shows the change in the hardness of the LPBF-fabricated samples at different conditions of heat treatment. The average hardness of the AM sample was 460 HV. Fei Lei et al. [24] showed that the micro-hardness of the H13 steel printed by LPBF technology depends on the volumetric energy density,

which is related to the laser power, scanning speed, hatch spacing, and layer thickness. The annealing processes homogenized the microstructure of the printed sample and decreased the hardness of the steel. Increasing the annealing temperature (820–1020) °C at the same holding time lowered the hardness due to the decomposition of the martensite. The quenching process helped increase the hardness of the steel to the maximum of 787 HV, then the tempering process reduced it to 572 HV.

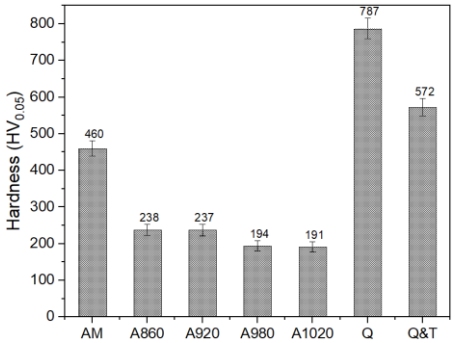

Fig. 3 Effect of heat treatment on the hardness of the LPBF-fabricated sample

Fig. 4 shows the cross-section image and hardness distribution profile from the surface to the core of the AM + Q&T + N sample. The nitriding process significantly increased the surface hardness of the steel samples up to 1012 HV due to the formation of nitride phases, such as CrN and $Fe_{3\text{-}4}N$, and the existence of carbide phases, including $Cr_{23}C_6$ and Fe_3C. The ferrite (α) and carbides detected in the XRD pattern are caused by the decomposition of the martensite (α') in the long-time tempering and nitriding processes. After nitriding was conducted at 520 °C for 3 h, the nitriding case depth reached the value of about 87 µm.

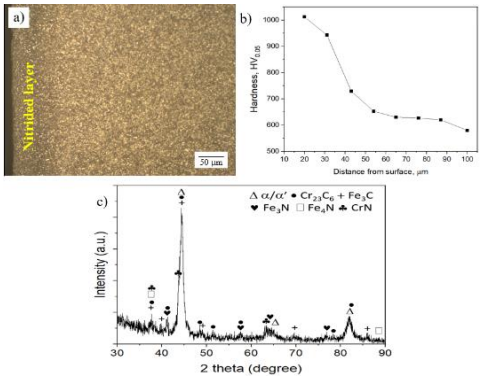

Fig. 4 a) Cross-section optical microscope image, b) micro-hardness distribution from surface to the core, and c) XRD analysis of the AM + Q&T + N sample

The microstructure evolution of the AM sample after quenching and tempering as well as nitriding processes was further investigated by the EBSD technique. The results of EBSD analysis in the core of the AM, AM + N, and AM + Q&T + N samples are presented in **Fig. 5**. The surface morphology of the samples could be distinguished from the SEM image (**Figs. 5 a1–c1**). On the polished surface of the AM sample, a cellular structure indicated by black arrows could be observed. A similar cell structure was also found on the surface of the AM + N sample. The cellular-dendritic structure of austenite, which was often observed in the AM sample of H13 steel [15], was formed at rapid solidification of the melt during LPBF. The cell boundary of austenite was often decorated by a dislocation network and nano-sized precipitation of refractory metal carbide [28]. During subsequent rapid cooling, the cellular austenite transformed into martensite and the cellular boundaries were inherited by the martensite as seen in the **Fig. 5a1**.

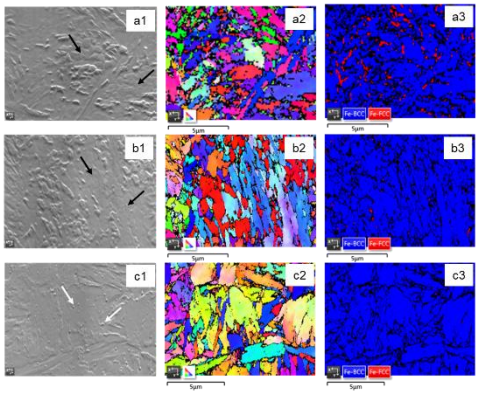

Fig. 5 Result of EBSD analysis showing the SEM image; the orientation map plotted for the AM building direction; and the phase map of the AM sample (a1–a3), AM + N sample (b1–b3), and AM + Q&T + N sample (c1–c3).

For the AM + Q&T + N sample, such a cellular structure did not appear, but many spherical particles indicated by white arrows emerged on the surface. They were the V-Mo-rich carbide particles, which is confirmed by the EPMA method in **Fig.6**, precipitate after a long time of heat treatment and nitriding processes. On the crystal orientation maps (**Figs. 5 a2–c2**), the blocks of lath martensite, which were surrounded by high-angle grain boundary, were coloured by the position of the building direction relative to the crystal orientation. A detailed description of the lath martensite block morphology has been reported elsewhere [29, 30].

The phase maps on **Figs. 5a3–c3** showed the distribution of retained austenite with face-centred cubic (FCC) crystal structure in the matrix of martensite with body-centred cubic (BCC) crystal structure. The black regions, where the crystal orientations could not be indexed, were mainly at the location of dense martensite boundaries or defects. In the AM sample, most of the retained austenite was observed at the boundaries between martensite blocks, but some were included inside martensite blocks. The powders were melted by laser beam scanning and solidified into the austenite phase, and the latter transformed into the martensite phase upon a rapid cooling process. A large amount of retained austenite and fine martensite block could be a consequence of the large cooling rate in LPBF. The very rapid solidification led to residual stress from the thermal contraction of austenite. During further rapid cooling below the martensite start temperature, the deformed austenite transformed into martensite. Due to the effect of deformation in austenite and the very high cooling rate, martensite is formed with very fine martensite blocks and a large amount of retained austenite [31-37]. Other researchers [38, 39] have also reported that the ratio of martensite to austenite depends a lot on laser power, scan speed, hatching pitch, and layer thickness.

Table 4 quantitatively shows the microstructure evolution of the AM sample after quenching and tempering as well as nitriding. Quantitative analyses of the EBSD data revealed the amount of

retained austenite and the average grain equivalent size of the martensite block in the samples. In the AM sample, a large amount of retained austenite was presented at the martensite block boundary. The size of the martensite block of this sample was also the smallest among the three samples. In the AM process, the effects of deformation in austenite and ultra-high cooling rate were combined, leading to significant refinement of martensite blocks and a large amount of retained austenite.

Table 4 Amount of retained austenite and martensite block size of the three samples

Sample	Retained austenite [%]	Martensite block size [μm]
AM	4.3 ÷ 5.4	1.6±1.2
AM + N	0.3 ÷ 0.5	2.1±1.5
AM + Q&T + N	0.0 ÷ 0.1	2.7±1.8

After nitriding was performed at 530 °C for 2 h (AM + N), the amount of retained austenite decreased substantially, and a few blocks of the retained austenite were present at the martensite grain boundaries. For the AM + Q&T + N sample, no retained austenite was detected by EBSD. The size of martensite blocks increased after nitriding in AM + N sample, but it was still finer than that in the AM + Q&T + N sample. The effects of nitriding or Q&T heat treatment on the microstructure of the AM samples can be interpreted as follows. During nitriding at 520 °C for 2h, low-temperature tempering occurred, in which the retained austenite decomposed, and the martensite recovered. That led to a decrease in retained austenite but an increase in martensite block size. The low temperature of tempering, however, did not promote the formation of V-Mo-rich carbides (**Fig. 5**). When Q&T heat treatment was applied to the AM steel, martensite of the as-built AM sample was replaced by a coarser martensite structure with precipitation of fine V-Mo-rich carbide, which was typically observed in the conventional sample of H13 steel (**Fig. 5c1-c3** and **Fig. 6**).

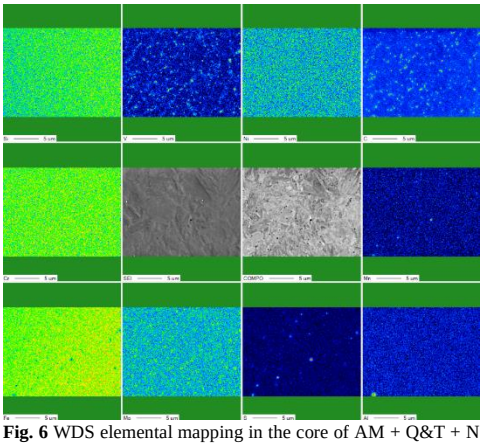

Fig. 6 WDS elemental mapping in the core of AM + Q&T + N sample

In **Fig. 6**, the change of carbide due to heat treatment processes was investigated by a field-emission electron probe microanalyzer equipped with wavelength dispersive spectroscopy (WDS). Elemental mapping by WDS could not detect the presence of carbide in the AM sample. When the AM sample was heated to 530 °C for nitriding, the tempering process occurred as the retained austenite decomposed and the martensite blocks slightly coarsened in the AM + N sample. However, the precipitation of carbides could not be detected by WDS mapping. At this nitriding temperature, the carbide precipitation was possibly too fine, which could not be seen with the 400 nm electron probe diameter used in the WDS measurement. In the AM + Q&T + N sample, the spherical particle that emerged on the polished surface was confirmed as V-rich carbide particles, and Mo was likely incorporated in those carbides. However, the presence of Cr-rich carbides could not be seen clearly. Probably, the Cr-rich carbides were present in the form of very fine particles, which could not be detected by WDS mapping on the as-polished surface of the sample.

CONCLUSIONS

After a sequence of the conventional heat treatment, the microstructure formed during the AM process was ruled out and replaced by the conventional microstructure. The following conclusions can be drawn from this study.

- The AM as-built AISI H13 steel sample had a microstructure consisting of very fine lath martensite, a significant amount of blocky retained austenite, and a small amount of carbide. The average hardness of the AM sample was 460 HV (~ 46 HRC), the density was 7.907 g/cm^3, and the porosity was 0.086 %.
- Increasing the annealing temperature (820–1020) °C increased the density but decreased the hardness and porosity of the sample. The hardness reached about 787 HV after quenching and about 572 HV after tempering processes. After gas nitriding was conducted, the nitride layer was formed, with a relatively high surface hardness of 1012 HV and a depth of nitriding layer of about 87 μm.
- Heat treatment and nitriding processes tended to increase the martensite block size, reduce the retained austenitic content, and precipitate the V-Mo-rich carbide in the 3D-printed AISI H13 steel.

Acknowledgements: This research is funded by the Hanoi University of Science and Technology (HUST) under project number T2021-SAHEP-015.

REFERENCES

1. M. Mazur, M. Leary, M. McMillan, J. Elambasseril, M. Brandt: Rapid Prototyping Journal, 22(3), 2016, 504–518. https://doi.org/10.1108/RPJ-06-2014-00752.
2. M. Åsberg, G. Fredriksson, S. Hatami, W. Fredriksson, P. Krakhmalev: Materials Science & Engineering A, 742, 2019, 584–589. https://doi.org/10.1016/j.msea.2018.08.046.
3. D. Manfredi, R. Bidulský: Acta Metallurgica Slovaca, 23 (3), 2017, 276-282. https://doi.org/10.12776/ams.v23i3.988.
4. R. Bidulsky, F. S. Gobber, J. Bidulska, M. Ceroni, T. Kvackaj, M. A. Grande: Metals, 11(11), 2021, 1831. https://doi.org/10.3390/met11111831.
5. P. Petrousek et al.: Acta Metallurgica Slovaca, 25, 2019, 283-290. https://doi.org/10.12776/ams.v25i4.1366.
6. J. Ålgårdh, A. Strondl, S. Karlsson, S. Farre, S. Joshi, J. Andersson, P. Nylén, A. Rashid, E. Hryha, L. Nyborg, N. Stenberg, A. Angré, O. Diegel, M. Schuisky, B. O. Bengtsson, H. Söderberg, S. Karamchedu, P. Emvin, F. Babou, S. Berg, P. Avdovic, M. Ahlfors, Å. Gustavsson, M. Åhlin, N. Eriksson, J. Ågren: *State-of-the-art for Additive Manufacturing of Metals*, Sweden: 2017
7. B. Redwood, F. Schöffer, B. Garret: *The 3D printing handbook: Technology, design and applications*, first ed., 3D Hubs B.V., 2017
8. I. Yadroitsev, I. Yadroitsava, A. D. Plessis, E. MacDonald: *Additive Manufacturing Materials and Technologies: Fundamentals of Laser Powder Bed Fusion of Metals*, first ed., Elsevier Inc., 2021

9. M. Wang, Y. Zhou, Q. S. Wei, Z. F. Fan: The Mechanical Behavior of AISI H13 Hot-Work Tool Steel Processed by Selective Laser Melting under Tensile Stress, The 29th Annual International Solid Freeform Fabrication Symposium, 2018, 1205–1212. http://dx.doi.org/10.26153/tsw/17119.
10. B. Almangour, D. Grzesiak, J. Yang: Journal of Materials Processing Technology, 244, 2017, 344–353. http://dx.doi.org/10.1016/j.jmatprotec.2017.01.019.
11. G. Telsang, J. D. Majumdar, G. Padmanabham, M. Tak, I. Manna: Surface & Coatings Technology, 258, 2014, 1108–1118. http://dx.doi.org/10.1016/j.surfcoat.2014.07.023.
12. R. Bidulsky et al.: Materials, 13, 2020, 3328; https://doi.org/10.3390/ma13153328.
13. G. Stornelli, D. Gaggia, M. Rallini, A. D. Schino: Acta Metallurgica Slovaca, 27, 2021, 122-126. https://doi.org/10.36547/ams.27.3.973.
14. C. J. Chen et al.: Journal of Materials Engineering and Performance, 26, 2017, 5577-5589. https://doi.org/10.1007/s11665-017-2992-0.
15. J. T. Wang, S. P. Liu, Y. P. Fang, Z. R. He: The International Journal of Advanced Manufacturing Technology, 108, 2020, 2453-2466. https://doi.org/10.1007/s00170-020-05584-4.
16. A. M. Vilardell et al.: Materials Science & Engineering A, 800, 2021, 140305.https://doi.org/10.1016/j.msea.2020.140305.
17. S. S. Akhtar, A. F. M. Arif, A. A. Abubakar: *Gas Nitriding of AISI H13 Steel Extrusion Dies: Consideration of Sharp Features in the Die Profiles*, AES-ATEMA'2014, Montreal, Canada, 2014.
18. D. Kovács, D. M. Kemény: Acta Metallurgica Slovaca, 27, 2021, 190-194. https://doi.org/10.36547/ams.27.4.1172.
19. [14.3.2023], Oerlikon Metco, H13 Hot Work Tool Steel Powder for Additive Manufacturing, https://www.oerlikon.com/ecoma/files/DSM-0322.1_AM_H13_Tool-Steel.pdf?download=true
20. G. Sander et al.: Corrosion, 74 (12), 2018, 1318-1350. https://doi.org/10.5006/2926.
21. G. B. Ko, W. S. Kim, K. J Kwon, T. K. Lee: Metals, 11, 2021, 516-537. https://doi.org/10.3390/met11030516.
22. B. Breidenstein, F. Brenne, L. Wu, T. Niendorf, B. Denkena: HTM Journal of Heat Treatment and Materials, 73, 2018, 173-186. https://doi.org/10.3139/105.110359.
23. E. Guenther, M. Kahlert, M. Vollmer, T. Niendorf, C. Greiner: Materials, 14, 2021, 928-938. https://doi.org/10.3390/ma14040928.
24. F. Lei, et al.: Materials, 15, 2022, 2686. https://doi.org/10.3390/ma15072686.
25. J. Bidulská, R. Bidulský, M. A. Grande, T. Kvačkaj: Materials, 12, 2019, 3724. https://doi.org/10.3390/ma12223724.
26. J. Bidulska, T. Kvackaj, R. Bidulsky, M. A. Grande: Acta Physica Polonica A, 122(3), 2012, 553-556. https://doi.org/10.12693/APhysPolA.122.553.
27. J. Bidulská, T. Kvačkaj, R. Bidulský, M. A. Grande, L. Litynska-Dobrzynska, J. Dutkiewicz: Chemicke Listy, 105(SI), 2011, s471-s473.
28. Y. T. Tang, et al.: Superalloy, 2020, 1055-1065. https://doi.org/10.1007/978-3-030-51834-9_103.
29. S. Morito, A. H. Pham, T. Ohba, T. Hayashi: Materials Today: Proceedings, 2S3, 2015, S913-S916. https://doi.org/10.1016/j.matpr.2015.07.430.
30. A. H. Pham, T. Ohba, S. Morito, T. Hayashi: Journal of Alloys and Compounds, 577S, 2013, S583-S586. https://doi.org/10.1016/j.jallcom.2012.02.008.
31. C. H. Li, X. Y. Li, W. C. Yu, J. Shi, M. Q. Wang, R. Wu: Journal of Materials Engineering and Performance, 11, 2022, 8711–8720. https://doi.org/10.1007/s11665-022-06985-0.
32. T. Wu, R. Wu, B. Liu, W. Liang, D. Q. Ke: Metals, 9(9), 2019, 958. https://doi.org/10.3390/met9090958.
33. M. Zorgani, C. Garcia-Mateo, M. Jahazi: Journal of Materials Research and Technology, 9(4), 2020, 7762-7776. https://doi.org/10.1016/j.jmrt.2020.05.062.
34. Y. X. Wang, Y. Tomota, T. Ohmura, S. Morooka, W. Gong, S. Harjo: Acta Materialia, 184, 2020, 30-49. https://doi.org/10.1016/j.actamat.2019.11.051.
35. K. I. Sugimoto, M. Itoh, T. Hojo, S. I. Hashimoto, S. Ikeda, G. Arai: Materials Science Forum, 539-543, 2007, 4309-4314. https://doi.org/10.4028/www.scientific.net/MSF.539-543.4309.
36. T. T. Xiong, J. P. Ren, C. J. Luo, R. Zuo: Journal of Physics: Conference Series, 2390, 2022, 012017. https://doi.org/10.1088/1742-6596/2390/1/012017.
37. G. S. Ansell, S. J. Donachie, R. W Messler: Metallurgical Transactions, 2, 1971, 2443–2449. https://doi.org/10.1007/BF02814881.
38. M. Narvan, K.S. Al-Rubaie, M. Elbestawi: Materials, 12(14), 2019, 2284-2304. https://doi.org/10.3390/ma12142284
39. M. Wang et al.: Metallurgical and Materials Transactions B, 50B, 2019, 531–542. https://doi.org/10.1007/s11663-018-1442-1.